

## ARTICLE OPEN



# Identifying inhibitors of epithelial–mesenchymal plasticity using a network topology-based approach

Kishore Hari<sup>1</sup>, Burhanuddin Sabuwala<sup>2</sup>, Balaram Vishnu Subramani<sup>3</sup>, Caterina A. M. La Porta<sup>4,5</sup>, Stefano Zapperi<sup>4,6</sup>, Francesc Font-Clos<sup>4,6</sup> and Mohit Kumar Jolly<sup>1</sup>✉

Metastasis is the cause of over 90% of cancer-related deaths. Cancer cells undergoing metastasis can switch dynamically between different phenotypes, enabling them to adapt to harsh challenges, such as overcoming anoikis and evading immune response. This ability, known as phenotypic plasticity, is crucial for the survival of cancer cells during metastasis, as well as acquiring therapy resistance. Various biochemical networks have been identified to contribute to phenotypic plasticity, but how plasticity emerges from the dynamics of these networks remains elusive. Here, we investigated the dynamics of various regulatory networks implicated in Epithelial–mesenchymal plasticity (EMP)—an important arm of phenotypic plasticity—through two different mathematical modelling frameworks: a discrete, parameter-independent framework (Boolean) and a continuous, parameter-agnostic modelling framework (RACIPE). Results from either framework in terms of phenotypic distributions obtained from a given EMP network are qualitatively similar and suggest that these networks are multi-stable and can give rise to phenotypic plasticity. Neither method requires specific kinetic parameters, thus our results emphasize that EMP can emerge through these networks over a wide range of parameter sets, elucidating the importance of network topology in enabling phenotypic plasticity. Furthermore, we show that the ability to exhibit phenotypic plasticity correlates positively with the number of positive feedback loops in a given network. These results pave a way toward an unorthodox network topology-based approach to identify crucial links in a given EMP network that can reduce phenotypic plasticity and possibly inhibit metastasis—by reducing the number of positive feedback loops.

*npj Systems Biology and Applications* (2020)6:15; <https://doi.org/10.1038/s41540-020-0132-1>

## INTRODUCTION

Metastasis, therapy resistance, and tumor relapse remain unsolved clinical challenges and major causes of cancer mortality<sup>1</sup>. During metastasis, cells navigate many bottlenecks: local invasion, intravasation, survival in circulation in matrix-deprived conditions, extravasation, and eventually colonization of the distant organ. Only a few (<0.02%) cells survive this cascade of events and are capable of initiating metastasis. Recent studies have identified phenotypic plasticity—the ability of cells to reversibly switch phenotypes in response to their ever-changing environmental conditions—as a hallmark of cancer metastasis<sup>2</sup>. Similarly, phenotypic plasticity enables a small proportion of cancers cells to transiently acquire an adaptive drug-refractory phenotype which may contribute to tumor relapse<sup>3</sup>. Therefore, identifying the mechanisms of phenotypic plasticity is essential for any major breakthroughs in cancer treatment.

Phenotypic plasticity is considered to be an adaptation strategy to survive in variable environmental conditions<sup>4</sup>. Recently, the contributions of phenotypic plasticity in driving metastasis and therapy resistance have been realized more prominently, especially due to the lack of any unique mutational signature being identified for cancer metastasis so far<sup>2</sup>, and the frequent emergence of resistance against targeted therapy<sup>3</sup>. Phenotypic plasticity, referred to as “the architect who never sleeps”<sup>5</sup>, can have various dimensions—metabolic plasticity<sup>6</sup>, epithelial–mesenchymal plasticity<sup>7</sup>, plasticity between cancer stem cell (CSC) and a non-CSC state<sup>8–10</sup>, and plasticity between drug-sensitive and drug-resistant/tolerant state<sup>11</sup> among others.

Cancer cells continually exploit phenotypic plasticity to adapt to their ever-changing environment by maximizing their fitness during cancer progression, metastasis, therapy resistance and eventually tumor relapse<sup>12</sup>. Moreover, phenotypic plasticity can amplify the non-genetic heterogeneity within tumors, thus increasing the number of “exit options” for cells in response to drugs, thereby increasing the versatility of the tumor cell population<sup>13</sup>. Thus, targeting phenotypic plasticity provides a unique opportunity to both curb cancer metastasis and to improve the efficiency of existing therapeutic strategies.

A canonical example of phenotypic plasticity is epithelial–mesenchymal plasticity (EMP), which involves partial and/or complete epithelial–mesenchymal transition (EMT) and/or mesenchymal–epithelial transition (MET). EMT and MET are embryonic developmental programs which are often adopted by cancer cells during metastasis<sup>14</sup>. EMT can fuel the dissemination of stationary cancer cells through reduced cell–cell adhesion and apico–basal polarity and increased migration and invasion. Conversely, MET may enable the disseminated cells that exit the bloodstream to survive in a different environment by regaining cell–cell adhesion and proliferation to eventually colonize that organ. EMT and MET were earlier thought of as binary processes (i.e. switching between epithelial and mesenchymal phenotypes), but recent *in vitro*, *in vivo* and *in silico* evidence strongly suggests that they are not “all-or-none” processes, and cells can stably reside in one or more hybrid E/M phenotypes, thus enabling various manifestations of EMP<sup>14</sup>. EMP can not only drive metastasis, but also influence the resistance to various

<sup>1</sup>Centre for BioSystems Science and Engineering, Indian Institute of Science, Bangalore 560012, India. <sup>2</sup>Department of Biotechnology, Indian Institute of Technology Madras, Chennai 600036, India. <sup>3</sup>School of Mathematics, Indian Institute of Science Education and Research, Thiruvananthapuram 695551, India. <sup>4</sup>Center for Complexity and Biosystems, University of Milan, 20133 Milano, Italy. <sup>5</sup>Department of Environmental Science and Policy, University of Milan, 20133 Milano, Italy. <sup>6</sup>Department of Physics, University of Milan, 20133 Milano, Italy. ✉email: mkjolly@iisc.ac.in

chemotherapeutic drugs and targeted therapies. It can also alter the tumor microenvironment to be immunosuppressive, eventually leading to overall poor survival of patients across cancer types<sup>15,16</sup>. Therefore, preventing the ability of cells to reversibly switch among these epithelial (E), mesenchymal (M), and hybrid E/M (H) phenotypes can have a significant clinical impact.

Most current preclinical and clinical efforts attempt to restrict EMP in only one direction—EMT or MET. Such efforts are likely to facilitate the transition in the opposite direction (i.e. MET or EMT respectively) and can possibly increase the frequency of hybrid E/M phenotypes which can be the “fittest” for metastasis<sup>17</sup>. Hence, these interventions may increase the metastatic load instead, depending on the phenotypic distribution of disseminated cells. Blocking EMP in both directions can overcome these potential side effects. Moreover, restricting EMP bidirectionally can also limit the ability of a clonal population to generate and/or maintain non-genetic heterogeneity<sup>18</sup>. Non-genetic heterogeneity can enable “bet-hedging” during the evolution of drug resistance<sup>19</sup>, as well as the co-existence of phenotypically distinct subpopulations of epithelial and mesenchymal cells that can communicate and cooperate among themselves to aggravate metastasis<sup>20,21</sup>. Thus, blocking EMP bidirectionally, or in other words “fixing cells at a given position on the epithelial–mesenchymal axis to prevent access to the range of states that might be required to facilitate different stages of the metastatic cascade”<sup>22</sup>, is likely to blunt the metastatic and drug-resistance potential of cancer cells much stronger than restricting only EMT or only MET.

Identifying ways to inhibit EMP requires a detailed mechanistic understanding of its dynamics. Experimentally, EMP can be tracked through recent advances such as live-cell imaging reporter constructs or single-cell RNA-seq and/or mass/flow cytometry<sup>13</sup>. Another approach to characterize the dynamics of EMP is by developing mechanism-based mathematical models of networks that have experimentally been identified to regulate EMT and/or MET. Many such mathematical models have helped gain useful insights into the dynamics of EMP and have driven the experiments to decode (a) how cells attain one or more hybrid E/M phenotype, (b) how reversible is EMP in both directions (E to M vs. M to E), and (c) whether cells take same or different paths en route EMT or MET<sup>23</sup>. However, none of these models investigated the possibility of identifying mechanisms to block EMP bidirectionally.

Here, we investigate the dynamics of various regulatory networks implicated in EMP and identify robust network topology-based design principles of EMP, using two different but complementary modeling formalisms—a discrete, parameter-independent method: asynchronous Boolean<sup>24</sup> and a continuous, parameter-agnostic method: RACIPE (Random Circuit Perturbation)<sup>25</sup>. Our results show that the phenotypic distributions that can be obtained through an EMP network depend majorly on network topology but are largely independent of specific kinetic parameters for each link in the network. We also pinpoint a set of network perturbations that can reduce EMP, and observe a unifying theme amongst them: a reduced number of total positive feedback loops embedded within an EMP network led to curtailed EMP. Therefore, our approach unravels the common operating principles of various EMP regulatory networks and offers a systematic framework to identify network perturbations to restrict EMP based on this network topology-based dynamical trait.

## RESULTS

RACIPE and Boolean models have similar phenotypic distributions for EMP networks

Boolean frameworks lack kinetic parameters and treat a gene to be discretely ON (1) or OFF (0), thus focusing on a coarse-grained view of how various interactions in a network can give rise to the

repertoire of dynamical behaviors<sup>26</sup>. RACIPE, on the other hand, generates an ensemble of continuous mathematical models (sets of coupled ordinary differential equations) with randomly chosen kinetic parameters for a given network topology and clusters the steady state solutions to identify the robust dynamical features of a given network. In other words, while a Boolean framework is parameter-independent, RACIPE can be thought of as a parameter-agnostic one.

Therefore, the similarities in dynamical traits of a network simulated via Boolean and RACIPE frameworks can unravel the extent to which the network topology drives the network dynamics, without much reliance on the specific choice of kinetic parameters. Across various EMP networks and the perturbations made in those, we have compared the outputs of these two modeling frameworks in terms of phenotypic distributions, and in ranking the effect of various perturbations in diminishing EMP (Fig. 1a).

We have investigated 6 different networks reported in EMP literature; these networks vary from 3 nodes to 8 nodes and 7 edges to 16 edges (Fig. 1b). First, we calculated the phenotypic distributions (i.e. stable steady state frequency distributions) obtained via RACIPE and Boolean models. To facilitate the comparison of Boolean and RACIPE models, we have discretized the output of RACIPE (as described in “Methods” section). First, we determined the sample size of parameter sets to be chosen for RACIPE, and the number of initial conditions for Boolean models, using a quantitative convergence analysis.  $N = 10,000$  was chosen as the optimal number of parameter sets for RACIPE, and as the optimal number of initial conditions for Boolean analysis, based on observed standard deviation in steady state distributions obtained from RACIPE and Boolean models (Fig. 2a, S1a).

For the miR-200/ZEB/ SNAIL/GRHL2 network (hereafter called as ‘GRHL2 network’; 4 nodes, 7 edges), a maximum of  $2^3 = 8$  stable steady states are possible (value of each node = 0 or 1; SNAIL is an input to the circuit), in discretized RACIPE and Boolean framework. From Boolean analysis, we obtained four stable states for this network across different numbers of initial conditions chosen. Two out of these four states were more prominent—(ZEB = 0, miR-200 = 1, GRHL2 = 1) and (ZEB = 1, miR-200 = 0, GRHL2 = 0)—than the others (Fig. 2a). These two states can be construed as epithelial (high miR-200 and GRHL2, low ZEB) and mesenchymal (low miR-200 and GRHL2, high ZEB) phenotypes as observed experimentally<sup>27,28</sup>. Discretized analysis of RACIPE results also identifies these four stable steady states with similar relative frequency as seen in the case of Boolean model, and 3 other states with relatively less frequencies (Fig. 2a). Put together, these results suggest that epithelial and mesenchymal phenotypes are the two most commonly expected phenotypes from the dynamics of GRHL2 network.

GRHL2 and OVOL1/2 are reported to play similar roles in inducing MET and/or inhibiting EMT<sup>29–31</sup>. Thus, epithelial (ZEB = 0, miR-200 = 1, OVOL = 1) and mesenchymal (ZEB = 1, miR-200 = 0, OVOL = 0) phenotypes are seen consistently as the most predominant ones in the RACIPE and Boolean model results for the SNAIL/miR-200/ZEB/OVOL network as well (Fig. S1a). Since GRHL2 can self-activate<sup>32</sup> and OVOL can self-inhibit<sup>33</sup>, we studied networks with GRHL2 self activation (referred to as GRHL2wa) and with and without OVOL self-inhibition (OVOL and OVOLsi respectively) (Fig. 1b). In both Boolean and RACIPE, we observed that epithelial and mesenchymal states were the highest frequency phenotypes across these 3 cases (Fig. S1b–d).

For the SNAIL/miR-200/ZEB/OCT4/miR-145 network (hereafter referred to as “OCT4” network; 5 nodes, 10 edges), a maximum of  $2^4 = 16$  stable steady states are possible (value of each node = 0 or 1; SNAIL is an input to the circuit). Boolean analysis across different numbers of initial conditions identified six out of the 16 possible states as stable steady states. The most predominant phenotypes were (ZEB = 0, miR-200 = 1, miR-145 = 0, OCT4 = 0)

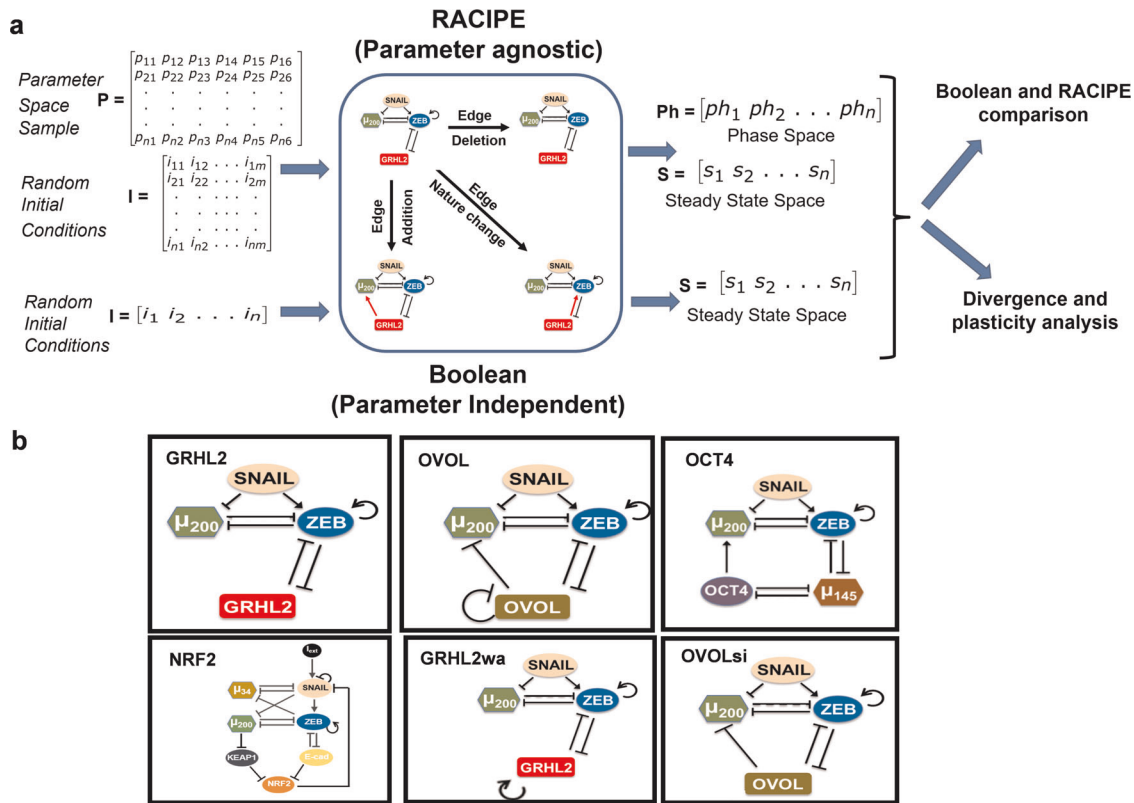


**Fig. 1** Dynamical approaches to investigate EMP. **a** Schematic of network analysis strategy. The top part of the figure depicts RACIPE methodology of sampling random parameter sets (matrix  $P$ ) and for each parameter set (each row in the matrix), randomly sampling multiple initial conditions to obtain steady states space and the phase space, i.e., information about monostable vs multi-stable parameter regions or phases. The bottom part of the figure depicts Boolean simulation method where for a given network, multiple initial conditions are randomly chosen and steady state space is obtained through asynchronous update. The center square depicts various possible topological perturbations done to the networks. **b** EMP networks analysed in the study, namely, GRHL2 (top-left, 4 nodes, 7 edges), OVOL (top-center, 4 nodes, 9 edges), OCT4<sup>29</sup> (top-right, 5 nodes, 10 edges), NRF2<sup>45</sup> (bottom-left, 8 nodes, 16 edges), GRHL2wa (bottom-center, 4 nodes, 8 edges) and OVOLsi<sup>29</sup> (bottom-right, 4 nodes, 8 edges).

and (ZEB = 1, miR-200 = 0, miR-145 = 1, OCT4 = 1), which can be mapped on to epithelial and mesenchymal states correspondingly. Results obtained via RACIPE analysis are qualitatively consistent with those from Boolean model; with some additional but less frequent states identified via RACIPE (Fig. S1b). Similar consistency is observed when comparing the phenotypic distributions for SNAIL/miR-200/ZEB/miR-34/NRF2/KEAP1 network (hereafter called as “NRF2 network”; Fig. S1g).

Next, for each of these different EMP networks, we quantified the difference between the phenotypic distributions obtained via RACIPE and Boolean models, using an information theory metric known as the Jensen–Shannon divergence (JSD). JSD measures the dissimilarity between two given probability distributions and varies between 0 and 1<sup>34</sup>; the larger the JSD, the more dissimilar or further apart are the two frequency distributions (Fig. 2b). JSD for Boolean vs. RACIPE solutions for the EMP networks modelled here varies between 0.05 and 0.27 (Figs 2c–e; S1e–f; S1h), suggesting a good quantitative agreement between the two methods. Thus, these results indicate that the phenotypic distributions enabled by these EMP networks are largely a feature of the underlying network topology rather than of specific kinetic parameters.

Quantifying the effect of edge perturbations on phenotypic distributions of EMP networks via JSD

To characterize the effects of network topology on phenotypic distributions further, we made changes to the topology in the form of single-edge perturbations and quantified the impact of these edge perturbations on the phenotypic distributions

obtained from various EMP networks. An edge perturbation can be one of the following: (a) deleting an edge, (b) adding a (hypothetical) edge, and (c) changing the sign of an edge (i.e. from activation to inhibition or vice versa). For a network with  $N$  nodes and  $E$  edges, there can be  $E$  edge deletions,  $2(N^2 - E)$  additions, and  $E$  changes in edge sign. Thus, for the “wild-type” (WT) SNAIL/miR-200/ZEB/GRHL2 network, 31 such perturbations are possible (Table S1), each of which will generate a new network topology. For every perturbation, we simulated the new network using both RACIPE and Boolean models and obtained the two corresponding phenotypic distributions. For the 32 distributions (31 perturbed + 1 “wild-type”) obtained via Boolean models, we then calculated the JSD between every two phenotypic distributions to identify perturbations that can drastically alter the phenotypic landscape. The network where the link from ZEB to GRHL2 was changed from inhibition to activation/excitation (ZEB-GRHL2\_2-1) had the highest JSD from all remaining 31 networks (Fig. 3a). RACIPE models, in addition to ZEB-GRHL2\_2-1 identified another perturbation which stood out relative to others—the deletion of the inhibitory link from ZEB to miR-200 (Zeb-miR200\_2-0) (Fig. 3b). Similar analysis for the NRF2 network using Boolean analysis identified two key perturbations while RACIPE analysis identified two additional ones (Fig. S2a).

Further, we compared JSD between perturbed and “wild-type” networks, calculated via RACIPE and Boolean analysis (Figs 3c–e, S2b). While the values of JSD were different for Boolean and RACIPE methods, a positive correlation was observed between the JSD values across all six EMP networks considered here. Moreover, the strongest perturbation obtained via both methods showed

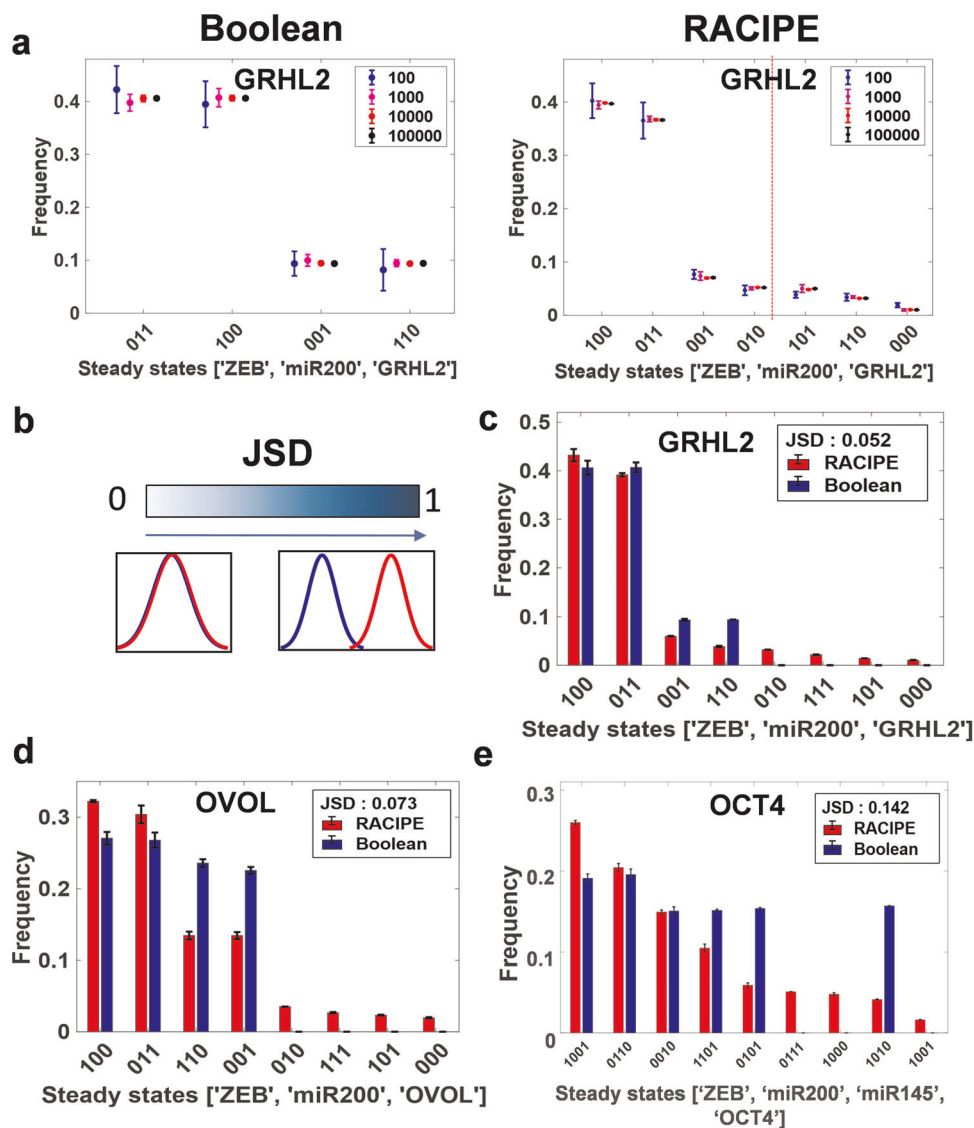


**Fig. 2** Comparing the outcomes of discrete (Boolean) and continuous (RACIPE) modelling frameworks. **a** Quantitative convergence of the state frequency landscape for different number of initial conditions in Boolean analysis (left) and different number of parameter sets randomly sampled from the parameter space for RACIPE (right) respectively. Error bars represent the mean  $\pm$  SD of the corresponding frequencies obtained by  $n = 3$  independent simulations. **b** Demonstration of JSD between two given probability distributions; JSD ranges from 0 to 1. **c**, **d**, **e** Comparison of phenotypic frequency distributions for different EMP networks, as obtained from Boolean and RACIPE.

concordance (highlighted by the arrows in Figs 3c–e and S2b). These results further emphasize the role of network topology in phenotypic distributions generated by EMP networks.

Correlation between JSD and phenotypic plasticity is not consistently significant across EMP networks

Next, we investigated whether the perturbed networks which are farthest from the “wild-type” network (i.e., having the highest JSD) are the ones with reduced phenotypic plasticity as well. Phenotypic plasticity is the ability of cells to sample multiple phenotypes and to switch from one phenotype to another, spontaneously or under external factors. The definition of phenotype in the present context can either be a stable steady state identified by mathematical simulations of EMP networks or a biological cell-state obtained by classifying the steady states based on marker expression levels. Hence, we define phenotypic plasticity in two different ways using RACIPE output. For every randomly chosen parameter set, RACIPE simulates the system with multiple, randomly chosen, initial conditions. For some parameter

sets, all chosen initial conditions converge to one stable state, while in others, multiple steady states (multistability) may be allowed. Thus, plasticity score 1 (PS1) is defined as the fraction of parameter sets that enable multistability (Fig. 4a). The definition of plasticity score 2 (PS2) is more biology-centric. We first define the “phenotype” of a given steady state based on the discretized expression levels of canonical epithelial and mesenchymal markers—miR-200 and ZEB, respectively<sup>27,35,36</sup>. This allows for the identification of various phases (combinations of co-existing steady states), such as the co-existence of epithelial and mesenchymal states {E,M} for instance. PS2 is the fraction of parameter sets which allow multiple phenotypic states, i.e. multi-stable phases (Fig. 4a). For a given network, we calculated PS1 and PS2 scores for the ‘wild-type’ and perturbed topologies; a comparison of these two metrics revealed a strong positive correlation across all six networks (Figs 4b; S3a). The perturbed networks had both increasing as well as decreasing effect on phenotypic plasticity (Figs 4b; S3a).

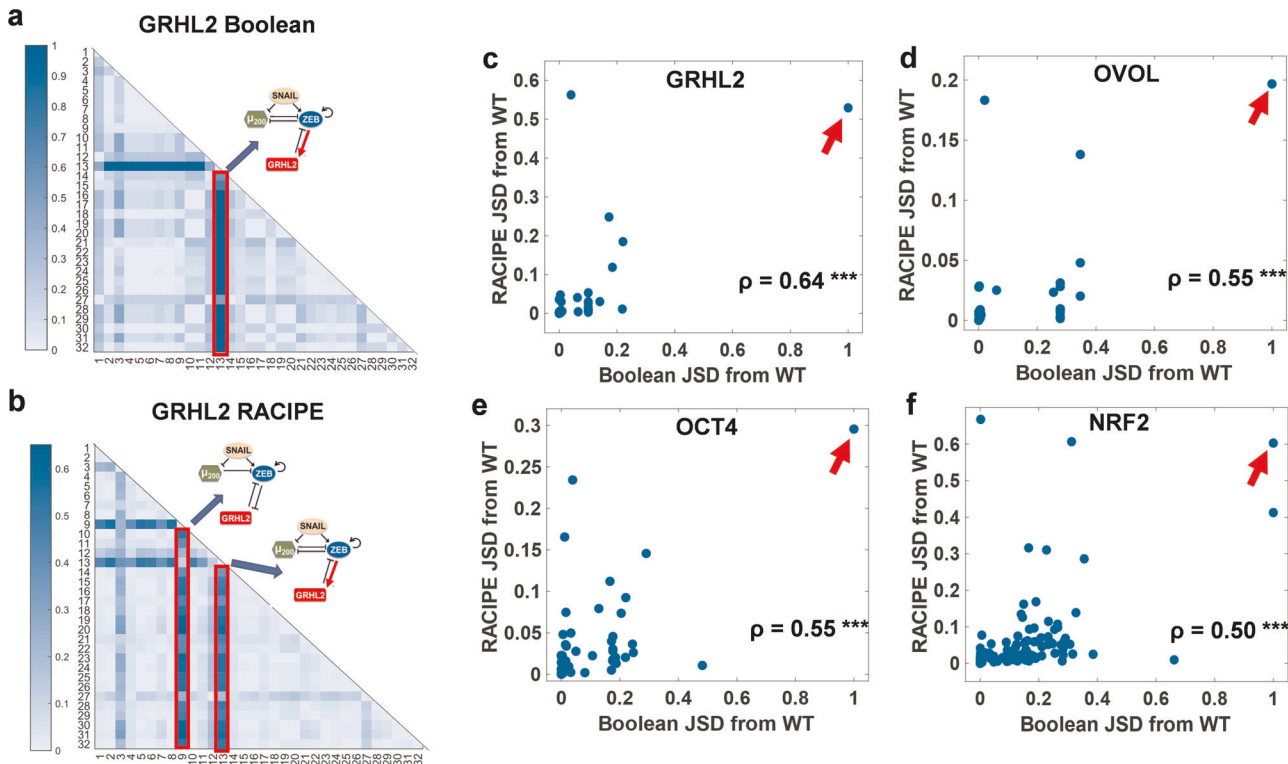


**Fig. 3** Quantifying the effect of single-edge perturbations on network behaviour landscapes. **a, b** Heatmap of the JSD between steady state distributions of all perturbations for the GRHL2 network from each other, obtained from **a** Boolean and **b** RACIPE. Color bar shows the value of JSD. Each number (1–32) represents a particular perturbed network except for number 2, which represents “wild-type” (Table S1). The perturbation highlighted in red has highest JSD from WT and most other perturbations. **c–f** Scatter plots of JSD between the steady state distributions of a perturbed network from WT as obtained via RACIPE vs. as obtained via Boolean. Each dot in a plot represents a perturbed topology for the EMP networks—**c** GRHL2, **d** OVOL, **e** OCT4, and **f** NRF2. The strongest perturbation identified by both Boolean and RACIPE is highlighted by the arrow. Spearman correlation coefficients ( $\rho$ ) are reported;  $***p < 0.001$ .

Further, we checked whether the topologies with the highest JSD from the ‘wild-type’ network led to a decrease or an increase in PS2 scores. We did not observe any significant overlap of the network topologies with the highest JSD vs. those with the highest or the lowest PS2 scores. This lack of trend was seen across all six networks considered (Fig. 5a). Further, a scatter plot between JSD from the “wild-type” network and fold-change in PS2 scores relative to the “wild-type” was plotted. While some networks showed a negative correlation, others had no significant correlation between these two metrics (Figs 5b; S3b). Similar results were obtained for analysis done using PS1 scores for these perturbed networks (Fig. S3c). Together, these observations suggest that JSD is not a good predictor of change in phenotypic plasticity.

Number of positive feedback loops in EMP networks correlates positively with phenotypic plasticity

Next, we revisited the network topologies with the highest JSD from the “wild-type” network to identify any topological signatures and observed that all of them were disrupting an overall positive feedback loop in the “wild-type”. Here, the “overall” sign of a loop is defined by the product of signs of edges (positive for activation, negative for inhibition) that form a cycle/loop; thus, a mutually inhibitory loop between two molecular players is effectively a positive feedback loop. In the GRHL2 network, the deletion of ZEB to miR-200 inhibitory link (*ZEB-miR200\_2-0*) disrupted the mutually inhibitory loop between ZEB and miR-200. Similarly, converting the inhibitory link from ZEB to GRHL2 to being excitatory (*ZEB-GRHL2\_2-1*) disrupted the mutually inhibitory feedback loop between ZEB and GRHL2 (Fig.

3a). In the NRF2 network, converting the inhibitory link from ZEB to E-cadherin to being excitatory (*ZEB-Ecad\_2-1*) disrupted the mutually inhibitory loop between ZEB and E-cadherin, and converting the inhibitory link from miR-200 to NRF2 to excitatory (*miR200-NRF2\_2-1*) disrupted the overall positive feedback loop formed by miR-200, KEAP1, NRF2 and SNAIL (Fig. S2a).

Previous analysis for simpler two-node networks has shown that mutually inhibitory and mutually excitatory loops (hence, both being overall positive loops) can lead to multistability which may drive phenotypic plasticity<sup>37,38</sup>. Such networks are typically observed underlying the cell-fate decisions during embryonic development<sup>39</sup>. Similar observations have been made for miR-200/ZEB feedback loop in driving trans-differentiation through EMP<sup>35,40</sup>. Therefore, we further inquired whether phenotypic plasticity can be correlated with the total number of positive feedback loops in a given network. We counted the number of positive feedback loops/cycles for all “wild-type” and perturbed topologies for all six EMP networks (see “Materials and Methods” for description). First, taking GRHL2 network as a case study, we showed that decreasing the number of positive feedback loops by one ( $WT - 1$ ) reduced phenotypic plasticity (Fig. 6a), while the reverse was true when the number of positive feedback loops was increased by one ( $WT + 1$ , Fig. 6a).

Next, we compared the number of positive feedback loops in each perturbed network with the corresponding plasticity score, using one-way ANOVA. Indeed, the mean plasticity score is higher for the groups of networks with higher number of positive feedback loops; this trend is observed across all six EMP networks in a statistically significant manner for both plasticity metrics—PS1, PS2 (Figs 6b; S4a–b), suggesting a correlation between the number of positive feedback loops in an EMP network, and its

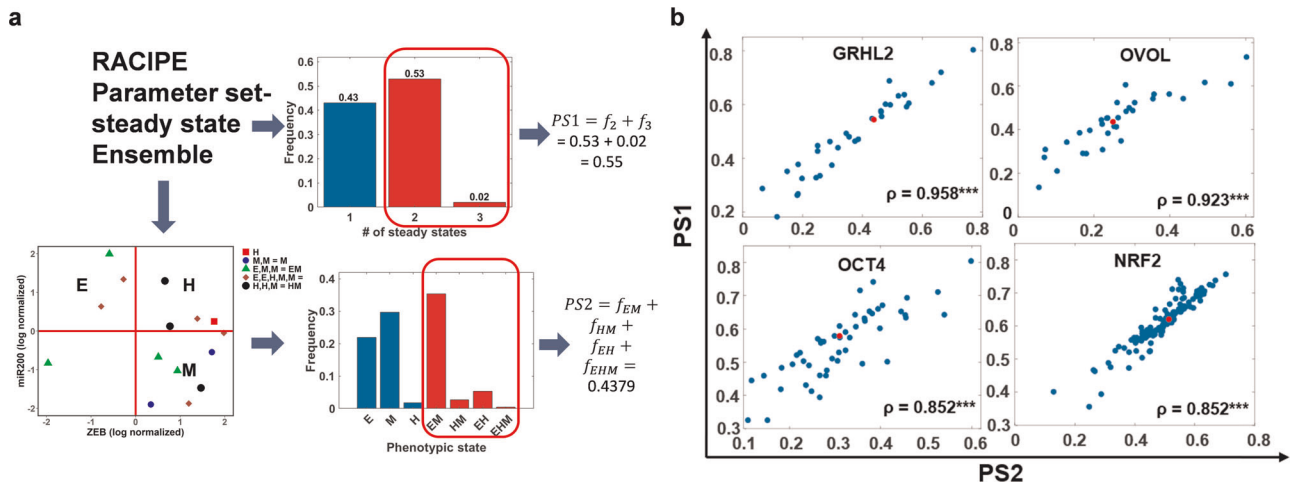


**Fig. 4 Metrics for quantifying phenotypic plasticity for the case of single-edge perturbations.** **a** Two definitions of plasticity: PS1 (top-right) is defined as the fraction of multi-stable parameter sets identified by RACIPE. PS2 (bottom) is calculated after ZEB and miR200 expression levels are used to classify steady states obtained from each parameter set (denoted by different colors) into Epithelial (E)—(high miR-200, low ZEB)/Hybrid (H)—(high miR-200, high ZEB)/Mesenchymal (M)—(low miR-200, high ZEB) phenotypes. Parameter sets are then characterized as monostable or multi-stable based on the phenotypic states they sample. PS2 is defined as the fraction of parameter sets giving rise to multiple phenotypes. **b** Scatter plot of PS1 vs. PS2 for different EMP networks - WT (colored red) and perturbed (colored blue; single-edge perturbed: edge deletion, edge nature change and edge additions) ones. Spearman correlation coefficients ( $\rho$ ) are denoted;  $***p < 0.001$ .

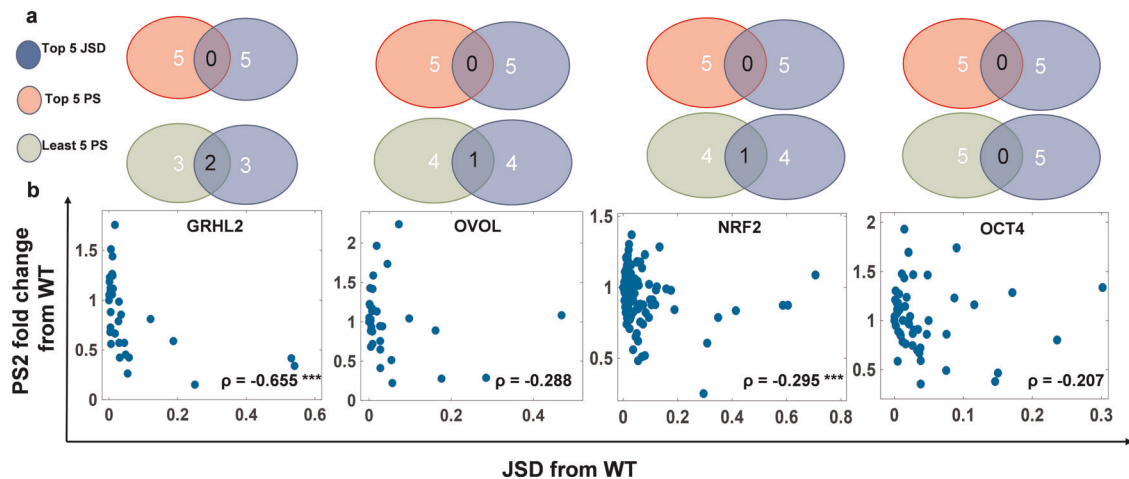


**Fig. 5 Correlation between JSD and phenotypic plasticity across EMP networks.** **a** Venn diagrams showing the extent of overlap among the perturbed networks that have the highest JSD from the “wild type” network and those with the highest or lowest fold change in plasticity scores (PS2). EMP networks shown are (from left to right): GRHL2, OVOL, NRF2 and OCT4. **b** Scatter plots for respective EMP networks. Each blue dot in a scatter plot is a perturbed network topology corresponding to that EMP network. Spearman correlation coefficient ( $\rho$ ) are denoted;  $***p < 0.001$ .

ability to give rise to phenotypic plasticity. We also observed that the total number of feedback loops (i.e., positive feedback loops + negative feedback loops) in the networks themselves did not exhibit any significant and consistent effect on plasticity, further emphasizing the role of positive feedback loops specifically (Fig. S5).

To test whether this observed correlation between plasticity scores and the number of positive feedback loops is specific to the network topology studied, we generated randomized topologies for each given network by swapping the edges in a given network (Fig. 6c). This procedure preserves the in-degree and out-degree of each node in the network but can change the distribution of excitatory or inhibitory links arriving at (in-degree) or originating from (out-degree) a given node. Thus, for a given EMP network, such randomization can generate various network topologies with varying number of net positive feedback loops. For each randomized network topology, we calculated PS1 and PS2.

Reinforcing our results to perturbed networks, we observed a positive trend between plasticity and positive feedback loops (Figs 6d; S4c, d), strengthening our hypothesis that the number of positive feedback loops in a given EMP network is a good predictor of phenotypic plasticity.

JSD, positive feedback loops, phenotypic plasticity and scalability of the corresponding trends

While the plasticity scores correlated positively with the number of positive feedback loops, there was heterogeneity in plasticity scores for a set of network topologies having the same number of positive feedback loops (Figs 6b, d; S4), indicating the presence of other factors in addition to positive feedback loops that determine phenotypic plasticity. Because a weak and inconsistent negative correlation was observed between JSD and plasticity scores

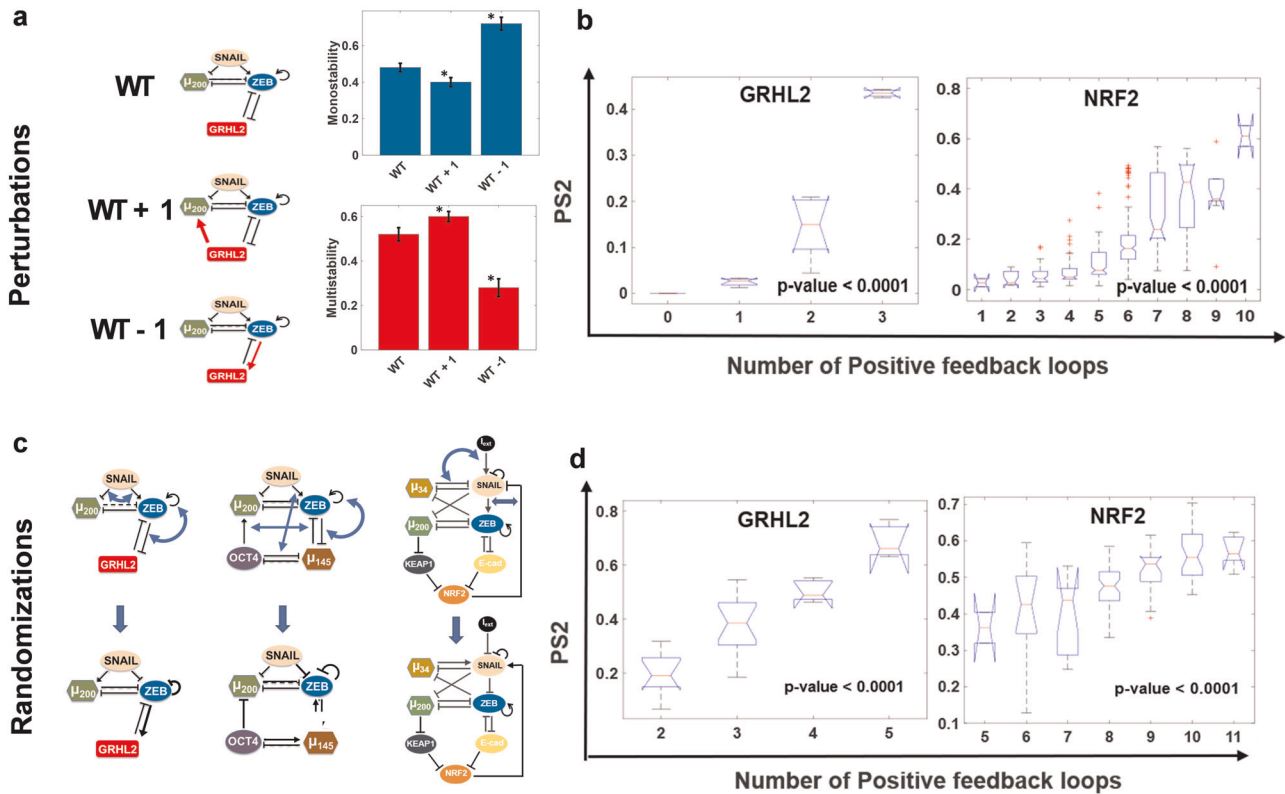


**Fig. 6 Effect of positive feedback loops on phenotypic plasticity in EMP networks.** **a** Demonstration of change in plasticity on altering the total number of positive feedback loops in GRHL2 network. Frequency of multi-stable parameters (PS2) increases as compared to WT upon the addition of positive feedback loop (GRHL2-miR200-ZEB-GRHL2) to the network (WT + 1) and reduces upon reduction of positive feedback loops by changing the GRHL2-ZEB-GRHL2 cycle to negative feedback (WT - 1). **b** Boxplots of PS2 vs. number of positive feedback loops for all the perturbed networks for GRHL2 and NRF2 networks. **c** Demonstration of network randomization (the in-degree and out-degree of each node is preserved; however, the number of inhibitory/excitatory nodes arriving at or emerging from a node are not necessarily conserved). **d** Same as B, but for randomized network topologies. p-value range for one-way ANOVA test are mentioned on the plots.

(Figs 5; S3b, c), we asked if JSD can contribute to explaining heterogeneity in plasticity.

For each network topology obtained by perturbing or randomizing the corresponding EMP network, we projected the plasticity score on a 2-D plot of its JSD from the wild-type and the number of positive feedback loops (Figs 7a, c; S6). These plots convey that JSD did not resolve the heterogeneity in plasticity scores of network topologies with the same number of positive feedback loops. To quantify this observation, we discretized JSD into ranges of values and calculated the correlation between positive feedback loops and plasticity for a range of JSD and correlation between JSD and plasticity for a fixed number of positive feedback loops.

The categorized JSD values maintained the lack of consistent correlation with plasticity (Fig. 7b, d) as seen earlier (Figs 5; S3b, c). The lack of correlation was not ameliorated by grouping of the network topologies by the number of positive feedback loops for either perturbed or randomized topologies. The correlation coefficient varied from -1 to 1 even within a given EMP network with many instances being statistically insignificant (Fig. 7e, g). On the other hand, when these network topologies were segregated based on JSD, plasticity scores and number of positive feedback loops were positively correlated across most ranges of the JSD values and across the six EMP networks (Fig. 7f, h). Together, these results strongly support positive feedback loops as good predictor of phenotypic plasticity and suggest that phenotypic frequencies may not be useful in measuring phenotypic plasticity.

To test the scalability of these results, we analysed two larger EMP networks: EMT\_RACIPE<sup>25</sup> (22 nodes, 72 edges, Fig. 8a) and EMT\_RACIPE<sup>24</sup> (26 nodes, 101 edges Fig. 8b), and all single-edge deletions and edge nature change (activation to inhibition and vice-versa) perturbations ( $n = 144$  and 202 respectively) for these networks. Given the network complexity, it becomes increasingly challenging to uniquely associate mathematically observed stable steady states with biological phenotypes. Hence, we used the generic definition of phenotypic plasticity (PS1). Similar to the smaller networks, the correlation observed between change in the number of positive feedback loops due to single-edge perturbations and the corresponding fold change in plasticity from WT was positive and significant (Fig. 8d, g). Similarly, the correlation between JSD and plasticity was weak and insignificant (Fig. 8c, f). Furthermore, the 2-D plots projecting plasticity scores onto JSD (x-axis) and change in positive feedback loops (y-axis) showed no distinct patterns (Fig. 8e, h), supporting the conclusion that JSD cannot reliably predict changes in phenotypic plasticity.

Owing to the huge number of positive feedback loops in these two networks, we were able to observe a saturation in the effect of the number of positive feedback loops on plasticity. Interestingly in these larger circuits, single-edge perturbations are capable of disrupting hundreds of positive feedback loops. The maximum number of positive loops disrupted by a single edge is ~1750 in EMT\_RACIPE and ~3000 in EMT\_RACIPE2, which account for more than 50% positive feedback loops in wild-type topology. Furthermore, two perturbations were observed in both networks that reduce the positive feedback loops by half or more (pointed

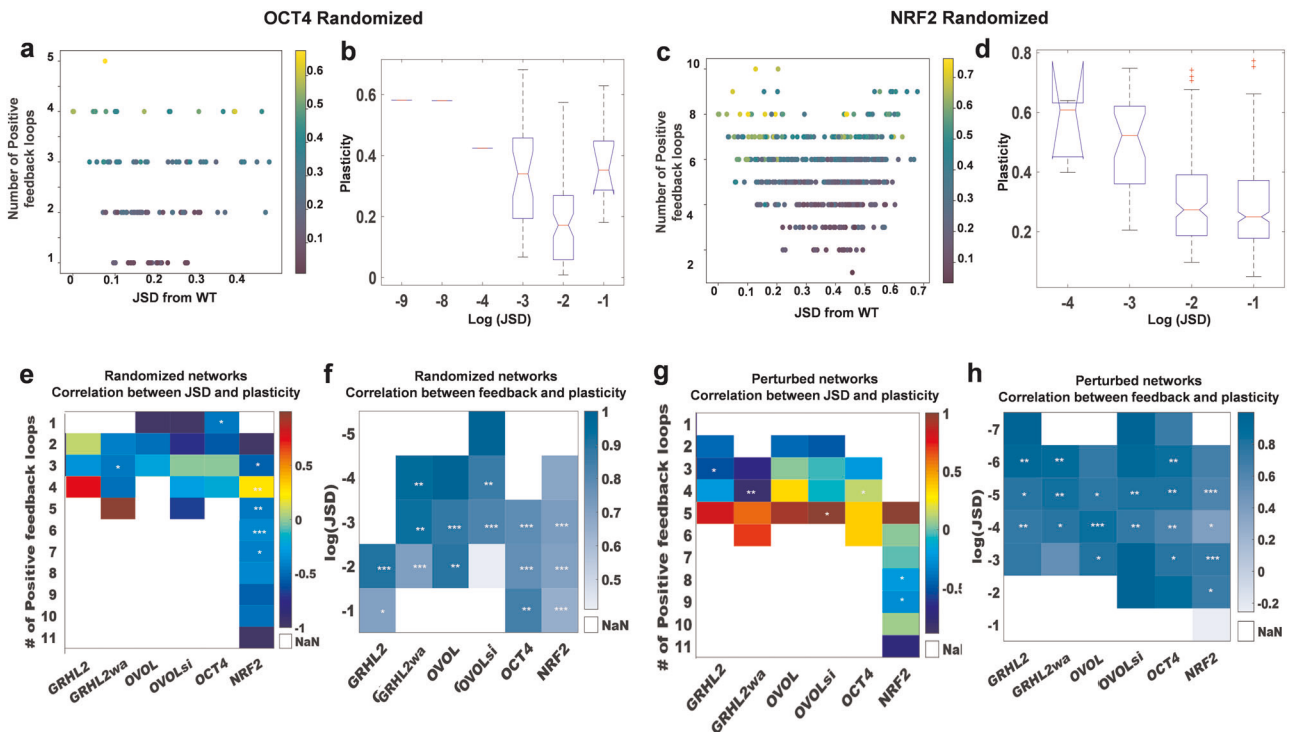


**Fig. 7 Correlation between JSD, plasticity, and number of positive feedback loops.** **a** PS2 for every randomized network for OCT4 module plotted as a function of its JSD from the WT network and number of positive feedback loops. Colorbar shows PS2 scores. **b** Boxplot for PS2 scores vs. range of JSD values for all networks plotted in **a**.  $p$ -value corresponds to one-way ANOVA test. **c, d** Same as **a, b** but for NRF2 module. **e** For each EMP module, all randomized networks are sub-categorized based on number of positive feedback loops. Each cell denotes correlation coefficient between JSD from WT and plasticity score fold change, wherever applicable (i.e. number of samples corresponding to that network and feedback loop count  $>3$ ). The white boxes (NaN) represent the cases with number of samples  $<3$ . Spearman correlation coefficient shown using color bar; significance represented as: \* $p < 0.05$ , \*\* $p < 0.01$ , \*\*\* $p < 0.001$ . **f** For each EMP module, all randomized networks are classified based on range of JSD values. Each cell denotes correlation coefficient between plasticity score fold change and number of positive feedback loops. **g, h** Same as **e, f** but for perturbed networks of each EMP module.

by red arrows), but only one of them significantly reduces plasticity. These observations, together with the observation that in smaller networks, multiple networks with the same number of positive feedback loops can have different levels of plasticity (Figs 6; S4) point towards additional network topological features that may contribute to determine the phenotypic plasticity resulting from EMP networks.

## DISCUSSION

Our ability to target phenotypic plasticity is limited by the understanding of its dynamics in tumors and the identification of tumor-specific molecular mechanisms driving it. While various transcriptional and epigenetic networks have been uncovered underlying phenotypic plasticity; how do these networks give rise to the co-existence of various drug-tolerant states, and the contribution of these different states to the minimal residual disease remains elusive<sup>41</sup>. Recent surge in our understanding of the dynamics of EMP has elucidated how the underlying EMP regulatory networks can give rise to various phenotypes/cell states along the spectrum of EMP, and how these different sub-populations may co-exist in a tumor and collaborate to drive tumor aggressiveness<sup>42</sup>. Nonetheless, targeting EMP in the clinic to observe a major reduction in metastasis still remains a challenge, because of lack of understanding of the precise spatio-temporal regulation of EMP involved during metastasis. Inhibiting one arm of EMP—say EMT—might actually promote MET and help colonization; and inhibiting MET may facilitate more dissemination<sup>7</sup>. Moreover, inhibiting only EMT or MET may drive the cells into one or more hybrid E/M phenotypes that are

considered to be the “fittest” for metastasis<sup>13</sup>. Therefore, while targeting EMP is important for restricting metastasis and therapy resistance, how to achieve that remains an unsolved challenge.

Our results present a computational platform to identify specific inhibitors for EMP using a network-level approach. We have simulated various networks identified to underlie EMP using different modeling strategies, to dissect the design principles underlying those networks; and suggest how perturbing those networks may prevent the ability of cells to switch back and forth among the E, M, and hybrid E/M phenotypes. Our analysis predicts that reducing the total number of positive feedback loops in the EMP network can restrict plasticity. A recent experimental study offers preliminary validation of this prediction, where disrupting the miR-200/ZEB mutually inhibitory (hence, an overall positive feedback) loop via CRISPR led to significantly reduced metastasis in vivo<sup>40</sup>. This feedback loop has been identified as a key regulator of EMP through extensive experimental and computational analysis<sup>27,35,36</sup>. Mathematical modeling for this loop has predicted how clonal cells responding to the same EMT-inducing signal can display different phenotypes due to the emergent multistability (the co-existence of multiple steady states/phenotypes), a prediction which was validated experimentally via single-cell analysis of EMP<sup>40</sup>. Various other EMP networks that have been mathematically studied have included various other direct or indirect positive feedback loops such as ZEB1/GRHL2<sup>28</sup>, ZEB1/ESRP1<sup>43</sup>, ZEB1/miR-1199<sup>44</sup>, or miR-34/SNAI1<sup>45</sup>.

Different modeling frameworks have been used to investigate the dynamics of EMP, depending on the size of network. While small-sized networks have typically been modelled via continuous approaches<sup>9,35,46–49</sup>, larger networks have been modelled via



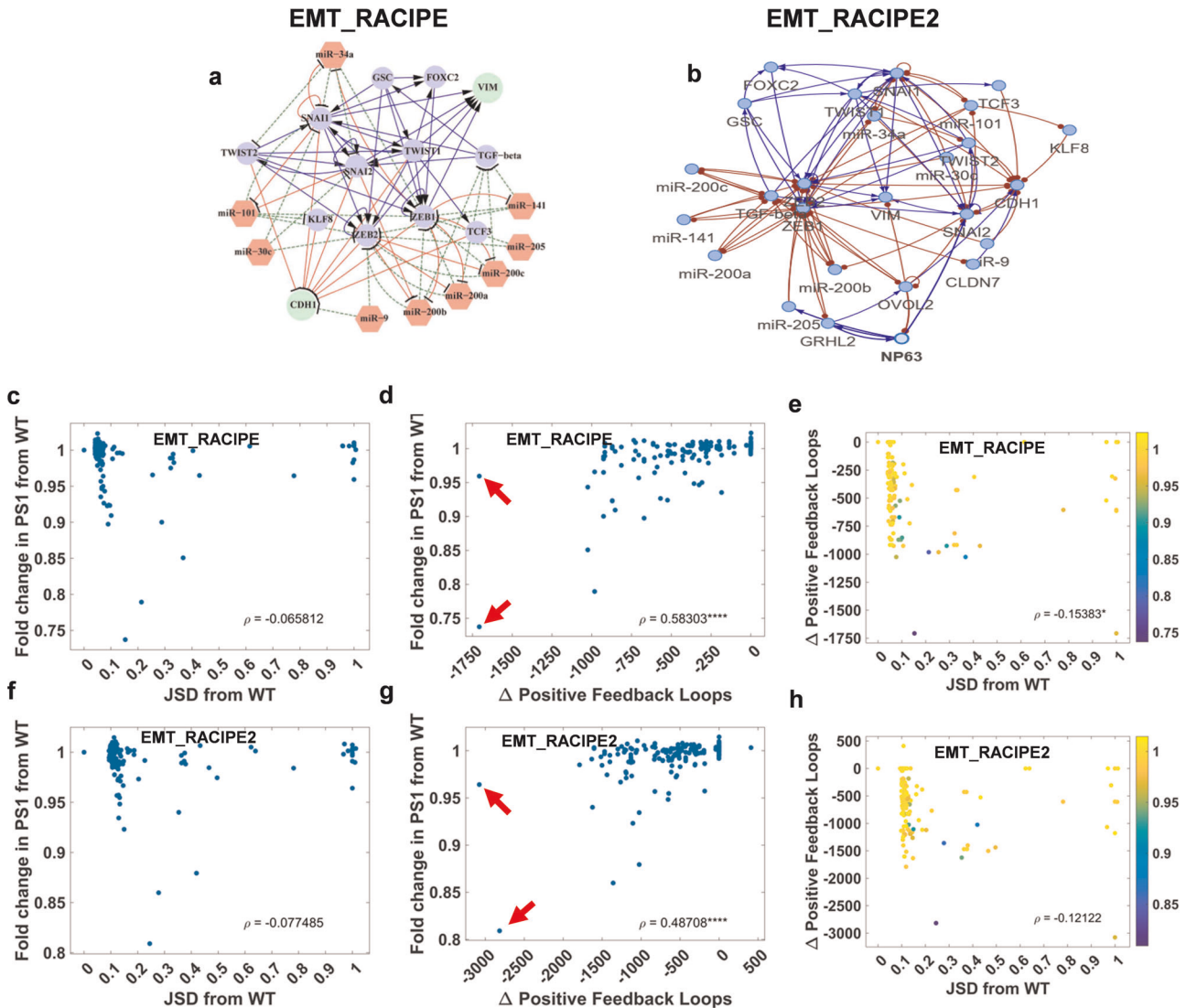


**Fig. 8** Analysis of 22 and 26 node networks. **a, b** The 22 node EMP network (EMT\_RACIPE) and 26 node EMP network (EMT\_RACIPE2). **c–e** EMT\_RACIPE (22 node, 72 edges). **c** Scatter plot between PS1 and change in total number of positive feedback loops of all the perturbations. **d** Scatter plot between PS1 and JSD of all perturbations from WT. **e** Scatter plot of JSD from WT and change in positive feedback loops for each perturbed network. Color code denotes absolute value of PS1 for a given perturbed network topology. **f–h** Same as **c–e** but for EMT\_RACIPE2.

discrete Boolean approaches due to lack of available kinetic parameters<sup>24,44,50,51</sup>. While continuous models provide a more quantitative mapping of system dynamics but require many kinetic parameters that can become experimentally intractable, Boolean modeling approaches provide a good estimate of qualitative behavior of a biochemical system without requiring a large set of parameters<sup>52</sup>, but are limited in terms of characterizing dynamic properties such as phenotypic plasticity and state transition rates. Thus, various efforts have been made to compare the dynamics of Boolean vs. continuous models and to integrate their strengths, particularly for capturing steady state distributions for smaller biological networks<sup>53–55</sup>.

Here, we compare the phenotypic distributions obtained for various EMP networks using Boolean formalism<sup>24</sup> and using RACIPE<sup>25</sup>. While Boolean tries to capture the phenotypes that can non-parametrically be observed in a network; RACIPE, by simulating networks for a large number of parameter sets, tries to capture the effect of parameteric variability observed in cell populations from one or multiple individuals on the phenotypes. Both methods infer network behavior as a function of the topological information, unbiased by any specific parameter set.

Hence, the qualitative and semi-quantitative agreement seen for Boolean and RACIPE models, across six EMP networks, enable us to understand the dynamics of EMP driven by network topology instead of specific kinetic parameter sets in a given cell/population. Furthermore, we could identify perturbations to the network topologies that affected the phenotypic distributions significantly across parameter sets. Thus, our method to identify network-topology-based predictions to inhibit EMP may provide an avenue to overcome a major bottleneck in targeted therapy—inter-individual variability in response. Moreover, through generating a larger number of randomized networks where the in-degree and out-degree of each node in the network was preserved, we showed that the phenotypic distributions and plasticity scores (PS1, PS2) obtained are specific to the particular topology of the networks regulating EMP. These results suggest evolutionary design principles of EMP networks that may have been optimized to induce EMP as/when needed during development/tissue regeneration, and stably maintain homeostatic differentiated phenotypes.

Intriguingly, the change in phenotypic plasticity, defined by both the plasticity scores does not correlate with JSD of

phenotypic distributions. One possible reason underlying this perceivably confounding result can be that the JSD only computes the distance between two steady state distributions; it does not capture information about whether the phenotypes can switch among themselves. (Spontaneous) phenotypic switching is facilitated by multi-stable phases, i.e. the co-existence of more than one stable steady state, for a given parameter set. Our results that the number of positive feedback loops in a given network determines the extent of phenotypic plasticity is reminiscent of reported connection between positive feedback loops and plasticity in other aspects of cancer too, where mutually inhibitory loops between two “master regulators” drive phenotypic switching<sup>56–59</sup>. Future efforts should aim at identifying which links(s) in the network to disrupt to cause maximal change in plasticity, because not every positive feedback loop may be equally likely to lead to multi-stability<sup>60,61</sup>. Moreover, for networks with the same number of feedback loops, the plasticity scores varied over a range, thus, identifying other predictors of plasticity based on network topology will be valuable. As an attempt to identify such complementary predictors, we investigated if JSD coupled with number of feedback loops can lead to isolate networks with highest plasticity, but no clear improvement in the trend was observed, eliminating JSD as a predictor of plasticity either individually or in combination with feedback loops.

Our results for the 22 and 26-node EMP network via RACIPE identified edge deletions that can reduce the positive feedback loops by half and have a significant impact on the plasticity. As more comprehensive networks representing the underlying biology are studied, RACIPE becomes too computationally expensive, and hence network theory-based measures to identify the feedback loop that, when disrupted, can have maximal effect in curbing plasticity would be valuable for future therapeutic applications.

It should be noted that while the existence of greater than or equal to two stable states is essential for phenotypic switching, we need to take into account the relative stability of these states, which determines the cellular transition rates from one state to another. In the context of EMP, hybrid epithelial mesenchymal states are known to be relatively less stable as compared to pure epithelial or pure mesenchymal states and hence are highly plastic<sup>62</sup>. Hybrid phenotypes are also associated with increased metastatic potential<sup>17,63</sup>. Thus, future efforts to restrict EMP bidirectionally should consider these state-specific traits to identify and rank various possible interventions to the EMP network topology.

Most of the targeted therapies in oncology target on disrupting a node in the network. Inevitably, most cells can identify “escape” routes by navigating various dimensions of the phenotypic plasticity landscape. Our results present an alternative and unorthodox mechanism to restrict the emergence of metastasis and drug resistance—breaking the feedback loops, i.e. targeting a link instead of a node, involved in phenotypic plasticity. Disrupting these feedback loops—the cornerstone of phenotypic plasticity—can restrict the ability of cancer cells to adapt to various therapeutic attacks and limit tumor aggressiveness.

## METHODS

### RANdom Circuit PERTurbation (RACIPE)

RACIPE<sup>25,64</sup> is a tool that simulates transcriptional regulatory networks (TRNs) in a continuous manner. Given a TRN, it constructs a system of Ordinary Differential Equations representing the network. For a given node  $T$  and a set of input nodes  $P_i$  and  $N_j$  that activate and inhibit  $T$ , respectively, the corresponding differential equation is given as Eq. (1).

$$\frac{dT}{dt} = G_T * \prod_i \frac{H^{S^+}(P_i, P_{iT}^0, n_{P_i,T}, \lambda_{P_i,T})}{\lambda_{P_i,T}} * \prod_j H^{S^-}(N_j, N_{jT}^0, n_{N_j,T}, \lambda_{N_j,T}) - k_T * T \quad (1)$$

**Table 1.** Parameter ranges used by RACIPE.

Parameters	Minimum	Maximum
Production rate ( $G$ )	1	100
Degradation rate ( $k$ )	0.1	1
Fold change (Inhibition $\lambda$ )	0.01	1
Fold change (Activation $\lambda$ )	1	100
Hill coefficient $n$	1	6
Threshold	The ranges depend on inward regulations—half functional rule	

Here,  $T$ ,  $P_i$  and  $N_j$  represent the concentrations of the species.  $G_T$  and  $k_T$  denote the production and degradation rates, respectively.  $P_{iT}^0$  is the threshold value of  $P_i$  concentration at which the non-linearity in the dynamics of  $T$  due to  $P_i$  is seen.  $n$  is termed as hill-coefficient and represents the extent of non-linearity in the regulation.  $\lambda$  represents the fold change in the target node concentration upon over-expression of regulating node. Finally, the functions  $H^{S^+}$  and  $H^{S^-}$  are known as shifted hill functions<sup>35</sup> and represent the regulation of the target node by the regulatory node (Eq. (2)).

$$H^{S^+/-}(B, B_A^0, n_{B,A}, \lambda_{B,A}) = \frac{B_A^{0n_{B,A}}}{B_A^{0n_{B,A}} + B^{n_{B,A}}} + \lambda * \frac{B^{n_{B,A}}}{B_A^{0n_{B,A}} + B^{n_{B,A}}} \quad (2)$$

Note that, for high values of the regulatory node concentration,  $H^{S^+/-}$  approaches  $\lambda$ .

For the model generated in this way, RACIPE randomly samples parameter sets from a pre-defined set of parameter ranges estimated from BioNumbers<sup>65</sup>. The ranges as reported by Huang et al.<sup>64</sup> are listed in Table 1.

At each parameter set, RACIPE integrates the model from multiple initial conditions and obtains steady states in the initial condition space. The output, hence, comprises of the collection of parameter sets and corresponding steady states obtained from the model. For the current analysis, we used a sample size of 10,000 for parameter sets and 100 for initial conditions. The parameters were sampled via a uniform distribution and the ODE integration was carried out using Euler’s method of numerical integration. Validation of the choice of the number of initial conditions and the integration methods is given in supplementary text (Fig. S7).

### Boolean simulations

For discrete analysis of our networks, the Boolean algorithm devised by Font-Clos et al.<sup>24</sup> was used. The nodes are updated asynchronously according to a majority rule such that the state of a node is set to 1 if the sum of activations to the node is more than the sum of inhibition and set to 0 if inhibition is more than activation. If inhibition and activations are equal, nodes are not updated. Steady state is said to have reached if the state of the network does not change over time-steps. The input for this formalism is a set of 10,000 initial conditions, which are randomly sampled from all possible states of the system and corresponding steady states.

### Discretization of RACIPE output and calculating the state frequency

For a given network with  $i = [1, n]$  nodes, the steady state expression levels of the nodes were normalized (Eqs. (3) and (4)).

$$E_{in} = (\log) 2 \left( \frac{E_i}{f_i} \right) \quad (3)$$

$$f_i = \frac{g_i}{k_i} \prod_j \lambda_{ij} \quad (4)$$

Where, for the  $i^{th}$  node,  $E_{in}$  is the normalized expression level,  $E_i$  is the steady state expression level,  $f_i$  is the normalization factor,  $g_i$  and  $k_i$  are production and degradation of the  $i^{th}$  node corresponding to the current steady state and  $\lambda_{ij}$  are the fold change in expression of  $i$  due to node  $j = [1, n]$ . The normalized expression levels of all steady states are then

converted into z-scores by scaling about their combined mean (Eq. (5)).

$$Z_i = \frac{E_{in} - \bar{E}_{in}}{\sigma_{in}} \quad (5)$$

where  $\bar{E}_{in}$  is the combined mean and  $\sigma_{in}$  is the combined variance.

The z-scores are then classified based on whether they are negative or positive into 0 (low) and 1 (high) expression levels, respectively. Each steady state of the network is thus labelled with a string of 1's and 0's, discretizing the continuous steady state levels. We then calculate the total frequency of each discrete state by counting the occurrence in all the parameter sets. For parameter sets with  $n$  steady states, the count of each steady state is taken as  $1/n$ , invoking the assumption that all the states are equally stable.

### Quantitative convergence

To estimate the optimal sample size of parameter sets for RACIPE and that of initial conditions for Boolean models, all networks were simulated at different sample sizes in triplicates and the mean and variance of the steady state frequency distribution was calculated. In all, 10000 was estimated as the ideal sample sizes for both methods as it was the smallest sample size for which the variance in steady state frequencies was minimum and the mean of the same was consistently similar to that of higher sample sizes.

### Jensen–Shannon divergence to measure distance between phenotypic distributions

To quantify the difference between two phenotypic distributions, an information theory metric, known as the JSD<sup>34</sup> was used, calculated for any two discrete frequency distributions  $P(x)$  and  $Q(x)$  as:

$$JSD(P||Q) = \frac{1}{2}D(P||M) + \frac{1}{2}D(Q||M) \quad (6)$$

where  $M = \frac{1}{2}(P + Q)$  and  $D$  denotes the Kullback-Leibler divergence (Eq. (7)).

$$D(P||Q) = \sum_{x \in K} P(x) \log \left( \frac{P(x)}{Q(x)} \right) \quad (7)$$

The metric, JSD, varies between 0 and 1 when the base 2 logarithm is used for calculation, with 0 indicating identical distributions and 1 indicating no overlap between the two distributions. The JSD calculations were done using the JSD function from *phylentropy* package in R 3.6.

### Calculating the number of positive feedback loops in a network

We estimated the number of feedback loops in the networks using the *networkx* module in Python 3.7, where a feedback loop is defined as a path traversed along the edges of a network that originates and ends at the same node. We then combine the nature of edges in each feedback loop to determine whether the given feedback loop is positive or negative. For example, in the OCT4 network (Fig. 1b), ZEB-miR200-ZEB is a positive feedback loop, as it goes through 2 inhibitory edges. On the other hand, ZEB-miR145-OCT4-miR200-ZEB is a negative feedback loop, as the edges involved are inhibition-inhibition-activation-inhibition, in that order.

### Statistical tests

All correlation analysis was done using Spearman correlation method using "cor" function in MATLAB R2018b (Mathworks). The corresponding statistical significance values are represented by \*, to be translated as: \* $p < 0.05$ , \*\* $p < 0.01$ , \*\*\* $p < 0.001$ . One-way ANOVA test was performed using *anova1* function in MATLAB R2018b (Mathworks).

### Reporting summary

Further information on research design is available in the Nature Research Reporting Summary linked to this article.

### DATA AVAILABILITY

The raw data generated for this study is available from the corresponding author (MKJ) upon reasonable request. Derived datasets supporting the current findings are available on the github page: [https://github.com/csbBSSE/Phenotypic\\_plasticity](https://github.com/csbBSSE/Phenotypic_plasticity).

### CODE AVAILABILITY

The package used for Boolean simulations is available at <https://github.com/ComplexityBiosystems/bmodel>. The custom functions written for analysis of RACIPE and Boolean data, including normalization, phenotypic distributions and plasticity are available on the github page: [https://github.com/csbBSSE/Phenotypic\\_plasticity](https://github.com/csbBSSE/Phenotypic_plasticity).

Received: 11 December 2019; Accepted: 9 April 2020;

Published online: 18 May 2020

### REFERENCES

- Ben-Jacob, E., Coffey, D. S. & Levine, H. Bacterial survival strategies suggest rethinking cancer cooperativity. *Trends Microbiol.* **20**, 403–410 (2012).
- Celià-Terrassa, T. & Kang, Y. Distinctive properties of metastasis-initiating cells. *Genes Dev.* **30**, 892–908 (2016).
- Boumahdi, S. & de Sauvage, F. J. The great escape: tumour cell plasticity in resistance to targeted therapy. *Nat. Rev. Drug Discov.* <https://doi.org/10.1038/s41573-019-0044-1> (2019).
- Xue, B. K. & Leibler, S. Benefits of phenotypic plasticity for population growth in varying environments. *Proc. Natl Acad. Sci. USA.* **115**, 12745–12750 (2018).
- Varga, J., De Oliveira, T. & Greten, F. R. The architect who never sleeps: Tumor-induced plasticity. *FEBS Lett.* **588**, 2422–2427 (2014).
- Lehüede, C., Dupuy, F., Rabinovitch, R., Jones, R. G. & Siegel, P. M. Metabolic plasticity as a determinant of tumor growth and metastasis. *Cancer Res.* **76**, 5201–5208 (2016).
- Bhatia, S., Monkman, J., Toh, A. K. L., Nagaraj, S. H. & Thompson, E. W. Targeting epithelial-mesenchymal plasticity in cancer: Clinical and preclinical advances in therapy and monitoring. *Biochem. J.* **474**, 3269–3306 (2017).
- Gupta, P. B. et al. Stochastic state transitions give rise to phenotypic equilibrium in populations of cancer cells. *Cell* **146**, 633–644 (2011).
- Jolly, M. K. et al. Coupling the modules of EMT and stemness: a tunable stemness window model. *Oncotarget* **6**, 25161–25174 (2015).
- Fumagalli, M. R., Lionetti, M. C., Zapperi, S. & LaPorta, C. A. M. Cross-Talk Between circRNAs and mRNAs modulates MiRNA-mediated circuits and affects melanoma plasticity. *Cancer Microenviron.* <https://doi.org/10.1007/s12307-019-00230-4> (2019).
- Goldman, A. et al. Temporally sequenced anticancer drugs overcome adaptive resistance by targeting a vulnerable chemotherapy-induced phenotypic transition. *Nat. Commun.* **6**, 6139 (2015).
- Gupta, P. B., Pastushenko, I., Skibinski, A., Blanpain, C. & Kuperwasser, C. Phenotypic plasticity: driver of cancer initiation, progression, and therapy resistance. *Cell Stem Cell* **24**, 65–78 (2019).
- Jolly, M. K. & Celià-Terrassa, T. Dynamics of phenotypic heterogeneity during emt and stemness in cancer progression. *J. Clin. Med.* **8**, 1542 (2019).
- Nieto, M. A., Huang, R. Y., Jackson, R. A. & Thiery, J. P. EMT: 2016. *Cell* **166**, 21–45 (2016).
- Dongre, A. & Weinberg, R. A. New insights into the mechanisms of epithelial-mesenchymal transition and implications for cancer. *Nat. Rev. Mol. Cell Biol.* **20**, 69–84 (2019).
- Yuan, S., Norgard, R. J. & Stanger, B. Z. Cellular plasticity in cancer. *Cancer Discov.* **9**, 837–851 (2019).
- Jolly, M. K., Mani, S. A. & Levine, H. Hybrid epithelial/mesenchymal phenotype(s): The 'fittest' for metastasis? *Biochim. Biophys. Acta Rev. Cancer* **1870**, 151–157 (2018).
- Tripathi, S., Chakraborty, P., Levine, H. & Jolly, M. K. A mechanism for epithelial-mesenchymal heterogeneity in a population of cancer cells. *PLOS Comput. Biol.* **16**, e1007619 (2020).
- Salgia, R. & Kulkarni, P. The genetic/non-genetic duality of drug resistance in cancer. *Trends Cancer* **4**, 110–118 (2018).
- Neelakantan, D. et al. EMT cells increase breast cancer metastasis via paracrine GLI activation in neighbouring tumour cells. *Nat. Commun.* **8**, 15773 (2017).
- Tsuji, T. et al. Epithelial-mesenchymal transition induced by growth suppressor p12 CDK2-AP1 promotes tumor cell local invasion but suppresses distant colony growth. *Cancer Res.* **68**, 10377–10386 (2008).
- Williams, E. D., Gao, D., Redfern, A. & Thompson, E. W. Controversies around epithelial-mesenchymal plasticity in cancer metastasis. *Nat. Rev. Cancer* **19**, 716–732 (2019).
- Jolly, M. K., Tripathi, S. C., Somarelli, J. A., Hanash, S. M. & Levine, H. Epithelial/mesenchymal plasticity: how have quantitative mathematical models helped improve our understanding? *Mol. Oncol.* **11**, 739–754 (2017).
- Font-Clos, F., Zapperi, S. & LaPorta, C. A. Topography of epithelial-mesenchymal plasticity. *Proc. Natl Acad. Sci. USA.* **115**, 5902–5907 (2018).

25. Huang, B. et al. Interrogating the topological robustness of gene regulatory circuits by randomization. *PLoS Comput. Biol.* **13**, e1005456 (2017).
26. Gómez, T. & Zaňudo, J. et al. Towards control of cellular decision-making networks in the epithelial-to-mesenchymal transition. *Phys. Biol.* **16**, 31002 (2019).
27. Brabletz, S. & Brabletz, T. The ZEB/miR-200 feedback loop—a motor of cellular plasticity in development and cancer? *EMBO Rep.* **11**, 670–677 (2010).
28. Mooney, S. M. et al. The GRHL2/ZEB feedback loop a key axis in the regulation of EMT in breast cancer. *J. Cell. Biochem.* **118**, 2559–2570 (2017).
29. Jolly, M. K. et al. Stability of the hybrid epithelial/mesenchymal phenotype. *Oncotarget* **7**, 27067–27084 (2016).
30. Jia, D. et al. OVOL guides the epithelial-hybrid-mesenchymal transition. *Oncotarget* **6**, 15436–15448 (2015).
31. Roca, H. et al. Transcription factors OVOL1 and OVOL2 induce the mesenchymal to epithelial transition in human cancer. *PLoS ONE* **8**, e76773 (2013).
32. Mehrazarin, S. et al. The p63 gene is regulated by grainyhead-like 2 (GRHL2) through reciprocal feedback and determines the epithelial phenotype in human keratinocytes. *J. Biol. Chem.* **290**, 19999–20008 (2015).
33. Nair, M., Bilanchone, V., Ortt, K., Sinha, S. & Dai, X. Ovol1 represses its own transcription by competing with transcription activator c-myc and by recruiting histone deacetylase activity. *Nucleic Acids Res.* **35**, 1687–1697 (2007).
34. Lin, J. Divergence measures based on the Shannon entropy. *IEEE Trans. Inf. Theory* **37**, 145–151 (1991).
35. Lu, M., Jolly, M. K., Levine, H., Onuchic, J. N. & Ben-Jacob, E. MicroRNA-based regulation of epithelial-hybrid-mesenchymal fate determination. *Proc. Natl. Acad. Sci. USA* **110**, 18144–18149 (2013).
36. Tian, X. J., Zhang, H. & Xing, J. Coupled reversible and irreversible bistable switches underlying TGF $\beta$ -induced epithelial to mesenchymal transition. *Biophys. J.* **105**, 1079–1089 (2013).
37. Chickarmane, V., Troein, C., Nuber, U. A., Sauro, H. M. & Peterson, C. Transcriptional dynamics of the embryonic stem cell switch. *PLoS Comput. Biol.* **2**, 1080–1092 (2006).
38. Gardner, T. S., Cantor, C. R. & Collins, J. J. Construction of a genetic toggle switch in *Escherichia coli*. *Nature* **403**, 339–342 (2000).
39. Zhou, J. X. & Huang, S. Understanding gene circuits at cell-fate branch points for rational cell reprogramming. *Trends Genet.* **27**, 55–62 (2011).
40. Celià-Terrassa, T. et al. Hysteresis control of epithelial-mesenchymal transition dynamics conveys a distinct program with enhanced metastatic ability. *Nat. Commun.* **9**, 5005 (2018).
41. Rambow, F. et al. Toward minimal residual disease-directed therapy in melanoma. *Cell* **174**, 843–855 (2018).
42. Jolly, M. K. et al. Hybrid epithelial/mesenchymal phenotypes promote metastasis and therapy resistance across carcinomas. *Pharmacol. Ther.* **194**, 161–184 (2019).
43. Jolly, M. K. et al. Interconnected feedback loops among ESRP1, HAS2, and CD44 regulate epithelial-mesenchymal plasticity in cancer. *APL Bioeng.* **2**, 031908 (2018).
44. Silveira, D. A. & Mombach, J. C. M. Dynamics of the feedback loops required for the phenotypic stabilization in the epithelial-mesenchymal transition. *FEBS J.* **287**, 578–588 (2020).
45. Jia, D. et al. Distinguishing mechanisms underlying EMT tristability. *Cancer Converg.* **1**, 2 (2017).
46. Bocci, F. et al. NRF2 activates a partial epithelial-mesenchymal transition and is maximally present in a hybrid epithelial/mesenchymal phenotype. *Integr. Biol.* **11**, 251–263 (2019).
47. Hong, T. et al. An Ovol2-Zeb1 mutual inhibitory circuit governs bidirectional and multi-step transition between epithelial and mesenchymal states. *PLoS Comput. Biol.* **11**, e1004569 (2015).
48. Huang, B. et al. Modeling the transitions between collective and solitary migration phenotypes in cancer metastasis. *Sci. Rep.* **5**, 17379 (2015).
49. Kang, X., Wang, J. & Li, C. Exposing the underlying relationship of cancer metastasis to metabolism and epithelial-mesenchymal transitions. *iScience* **21**, 754–772 (2019).
50. Steinway, S. N. et al. Network modeling of TGF $\beta$  signaling in hepatocellular carcinoma epithelial-to-mesenchymal transition reveals joint sonic hedgehog and Wnt pathway activation. *Cancer Res.* **74**, 5963–5977 (2014).
51. Steinway, S. N. et al. Combinatorial interventions inhibit TGF $\beta$ -driven epithelial-to-mesenchymal transition and support hybrid cellular phenotypes. *npj Syst. Biol. Appl.* **1**, 15014 (2015).
52. Wynn, M. L., Consul, N., Merajver, S. D. & Schnell, S. Logic-based models in systems biology: a predictive and parameter-free network analysis method. *Integr. Biol.* **4**, 1332–1337 (2012).
53. Saadatpour, A. & Albert, R. A comparative study of qualitative and quantitative dynamic models of biological regulatory networks. *EPJ Nonlinear Biomed. Phys.* **4**, 5 (2016).
54. Samaga, R. & Klamt, S. Modeling approaches for qualitative and semi-quantitative analysis of cellular signaling networks. *Cell Commun. Signal.* **11**, 43 (2013).
55. Wittmann, D. M. et al. Transforming Boolean models to continuous models: Methodology and application to T-cell receptor signaling. *BMC Syst. Biol.* **3**, 98 (2009).
56. Huang, B. et al. The three-way switch operation of Rac1/RhoA GTPase-based circuit controlling amoeboid-hybrid-mesenchymal transition. *Sci. Rep.* **4**, 6449 (2014).
57. Jia, D., Park, J., Jung, K., Levine, H. & Kaiparettu, B. Elucidating the metabolic plasticity of cancer: mitochondrial reprogramming and hybrid metabolic states. *Cells* **7**, 21 (2018).
58. Jolly, M. K. et al. Towards elucidating the connection between epithelial-mesenchymal transitions and stemness. *J. R. Soc. Interface* **11**, 20140962 (2014).
59. Saha, M. et al. AMPK-Akt double-negative feedback loop in breast cancer cells regulates their adaptation to matrix deprivation. *Cancer Res.* **78**, 1497–1510 (2018).
60. Cherry, J. L. & Adler, F. R. How to make a biological switch. *J. Theor. Biol.* **203**, 117–133 (2000).
61. Tiwari, A. & Igoshin, O. A. Coupling between feedback loops in autoregulatory networks affects bistability range, open-loop gain and switching times. *Phys. Biol.* **9**, 55003 (2012).
62. Pastushenko, I. & Blanpain, C. EMT transition states during tumor progression and metastasis. *Trends Cell Biol.* **29**, 212–226 (2019).
63. Kröger, C. et al. Acquisition of a hybrid e/m state is essential for tumorigenicity of basal breast cancer cells. *Proc. Natl. Acad. Sci. USA* **116**, 7353–7362 (2019).
64. Huang, B. et al. RACIPE: a computational tool for modeling gene regulatory circuits using randomization. *BMC Syst. Biol.* **12**, <https://doi.org/10.1186/s12918-018-0594-6> (2018).
65. Milo, R., Jorgensen, P., Moran, U., Weber, G. & Springer, M. BioNumbers—the database of key numbers in molecular and cell biology. *Nucleic Acids Res.* **38**, D750–D753 (2009).

## AUTHOR CONTRIBUTIONS

M.K.J. and F.-F.C. designed the research; C.L.P. and S.Z. analysed the data; K.H., B.S., and B.V.S. carried out the simulations; all authors discussed results and participated in the preparation of the paper; M.K.J. supervised the research.

## COMPETING INTERESTS

The authors declare no competing interests.

## ADDITIONAL INFORMATION

**Supplementary information** is available for this paper at <https://doi.org/10.1038/s41540-020-0132-1>.

**Correspondence** and requests for materials should be addressed to M.K.J.

**Reprints and permission information** is available at <http://www.nature.com/reprints>

**Publisher's note** Springer Nature remains neutral with regard to jurisdictional claims in published maps and institutional affiliations.



**Open Access** This article is licensed under a Creative Commons Attribution 4.0 International License, which permits use, sharing, adaptation, distribution and reproduction in any medium or format, as long as you give appropriate credit to the original author(s) and the source, provide a link to the Creative Commons license, and indicate if changes were made. The images or other third party material in this article are included in the article's Creative Commons license, unless indicated otherwise in a credit line to the material. If material is not included in the article's Creative Commons license and your intended use is not permitted by statutory regulation or exceeds the permitted use, you will need to obtain permission directly from the copyright holder. To view a copy of this license, visit <http://creativecommons.org/licenses/by/4.0/>.

© The Author(s) 2020